Materials Science

AIMS Materials Science, 3(2): 573-590.
DOI: 10.3934/matersci.2016.2.573
Received: 04 April 2016
Accepted: 09 May 2016
Published: 16 May 2016

http://www.aimspress.com/journal/Materials

Research article

Synthesis, characterization and quantitative analysis of porous metal microstructures: Application to microporous copper produced by solid state foaming

Mark A. Atwater [1], **Kris A. Darling** [2], **and Mark A. Tschopp** [2,*]

[1] Department of Applied Engineering, Safety and Technology, Millersville University, Millersville, PA, USA
[2] US Army Research Laboratory, Aberdeen Proving Ground, MD, USA

* **Correspondence:** Email: mark.a.tschopp.civ@mail.mil.edu; Tel: 1-410-306-0855.

Abstract: Porous metals can be created through a wide variety of processing techniques, and the pore morphology resulting from these processes is equally diverse. The structural and functional properties of metal foams are directly dependent on the size, shape, interconnectedness and volume fraction of pores, so accurately quantifying the pore characteristics is of great importance. Methods for analyzing porous materials are presented here and applied to a copper-based metallic foam generated through solid state foaming via oxide reduction and expansion. This process results in large voids (10s of microns) between sintered particles and small pores (10 microns to less than 50 nm) within particles. Optical and electron microscopy were used to image the porosity over this wide range, and the pore characteristics were quantified using image segmentation and statistical analysis. Two-dimensional pore analysis was performed using the Chan-Vese method, and two-point correlation and lineal path functions were used to assess three-dimensional reconstructions from FIB tomography. Two-dimensional analysis reveals distinct size and morphological differences in porosity between particles and within them. Three-dimensional analysis adds further information on the high level interconnectedness of the porosity and irregular shape it takes, forming tortuous pathways rather than spherical cells. Mechanical polishing and optical microscopy allow large areas to be created and analyzed quickly, but methods such as focused ion beam (FIB) sectioning can provide additional insight about microstructural features. In particular, after FIB milling is used to create a flat surface, that surface can be analyzed for structural and compositional information.

Keywords: microporous; metallic foam; FIB tomography; pore morphology; Chan-Vese method; two point correlation function; lineal path function

Abbreviations

2D: Two-Dimensional
3D: Three-Dimensional
AERO: Additive Expansion by the Reduction of Oxides
CCI: Channeling Contrast Imaging
CDF: Cumulative Density Function
LPF: Lineal Path Function
EBSD: Electron Backscatter Diffraction
EDS: Energy-Dispersive X-ray Spectroscopy
FIB: Focused Ion Beam
SEM: Scanning Electron Microscopy
TEM: Transmission Electron Microscopy
TPCF: Two Point Correlation Function

1. Introduction

In nature, porous materials (e.g., wood, pumice, and sponge) are ubiquitous. They possess a unique combination of properties, such as absorption, buoyancy, and good strength with low density that make them structurally and functionally advantageous. These advantages make synthetic analogues desirable as well, but efficiently creating and controlling porosity in engineered materials is an ongoing challenge. The difficulties encountered in producing these foamed materials (or more appropriately, *cellular solids* [1]) are hardly new. Metallic foams were first described early in the 20th century, but did not gain significant momentum until the late 1950s and 1960s when commercial operations began [2]. In reality, these "advanced" materials have been in development for nearly a century. Metallic foams continue to be scientifically interesting for use in structural applications and those involving filtration, catalysis, acoustic management, thermal management, and many other applications [3] that are uniquely satisfied by the combination of metallic properties with a reduced effective density.

Using these materials in demanding applications requires a fundamental understanding of their properties, so processing and characterizing these materials is significant for establishing the processing-structure-property relationships. Pore size and morphology, the degree of pore interconnectedness (coalescence) and the openness of the pores to the material surface (percolation) all play definitive roles in the mechanical and physical properties (e.g., [1,3,4]). For instance, foams with closed porosity are more suitable for structural applications, buoyancy, acoustic and thermal insulation and impact energy absorption. Open cell foams often serve in functional applications such as filtration, heat exchangers, catalyst support and other applications which benefit from the ability to flow substances through the pores and to utilize the increased surface area provided.

The porosity of metallic foams (and therefore the properties) is directly controlled by material parameters (e.g., alloy chemistry) and processing parameters (e.g., [4–9]). Since there is variety of desirable properties for metallic foams, the manufacturing schemes must also vary. The two primary manufacturing categories are liquid state and solid state foaming. Liquid state methods include direct (gas injection) and indirect (blowing agent) foaming of a metallic melt [7], casting over hollow spheres [10] and gas-metal eutectic reaction (gasars) [31,38]. Solid state methods for producing foam structures include electrodeposition [11–14], sintering around a fugitive template [1,15–21], dealloying [22,23,24] and gas entrapment [25–30]. Each of these methods creates porosity of varying size, morphology and volume fraction, so characterization methods must be tailored as well.

The properties of a metallic foam, structural and functional, are determined by the pore structure, so characterizing the porosity is a foundational step. In certain cases the porosity is designed by means of a sacrificial space holder, by sintering ordered arrays of hollow spheres or otherwise creating a regular size, shape and spacing of pores [26]. It is more common, however, that pore size and morphology resulting from commercial production techniques are random, and these stochastic foams present a greater need and challenge to be characterized, especially as pore size trends toward the nanoscale for surface-sensitive applications.

In this work, methods for characterizing porous metallic materials are presented, with a specific focus on a foamed metal microstructure created using a recently developed solid state foaming method referred to as the Additive Expansion by the Reduction of Oxides (AERO) process. This material presents an interesting case for characterization as it combines unique microstructural properties and multi-scale porosity ranging from tens of microns to tens of nanometers. Furthermore, the pore morphology is not dominated by spherical cells, but rather is comprised of a tortuous series of interconnected pathways. A variety of characterization and statistical analysis techniques have been used to describe this material. Samples were prepared through mechanical polishing and optical microscopy (Section 3.1) and by focused ion beam (FIB) sectioning and electron microscopy (Section 3.2). Porosity was assessed using image segmentation and statistical analysis, and FIB sections were also examined in regard to grain structure and composition. Alternative methods of characterizing porosity and related considerations are described in Section 4.

2. Materials and Method

A copper-antimony (Cu-Sb) alloy was created by mechanically alloying elemental powders of Cu and Sb (Alfa Aesar, 99.9% and 99.5%, respectively) for 4 h at cryogenic temperature (−196 °C) using a modified SPEX 8000M Mixer/Mill. The elemental powders were weighed and combined to achieve 5 at% Sb in Cu. The powders were stored and milled under Ar (less than 1 ppm O_2), but the as-received Cu contained approximately 5000 ppm O_2 according to the manufacturer’s certificate of analysis. This represents oxide content sufficient to cause the expansion of pores during annealing under a reducing atmosphere. The ball milling process was used to intimately mix the elements as well as to refine and distribute pre-existing oxides. The alloyed powder was annealed at 600 °C for a period of 1 h under 3% H_2 (bal. Ar) to achieve the porous structure. The working hypothesis of this mechanism is that the oxide particles are reduced by the hydrogen and produce steam which results in the expansion of a void at each oxide location. The foaming process progresses from external surfaces inward toward the center until all oxides have been reduced and the metal is fully foamed. These concepts and results are detailed in prior work on the AERO process [31].

Light microscopy was performed using a Nikon Epiphot 300 microscope, and samples were processed with consecutively finer grits of abrasive and final-polished with 0.5 μm alumina paste. Scanning electron microscopy (SEM) was carried out on loose powder (on carbon tape) using an FEI Nova Nano Lab 600 dual beam microscope. Cross-sectional preparation was performed using a focused ion beam (FIB). Analysis of grain size was conducted using FIB channeling contrast imaging (CCI). Chemical analysis was performed using energy-dispersive X-ray spectroscopy (EDS) area and line scans. Image processing was performed using Image J, and statistical analysis of the microstructural data was performed using MATLAB.

3. Results

The AERO process [32] creates a porosity of approximately 40% *within* powder particles, and results in approximately 67% overall porosity when first compacted into pellets and then expanded. The most unique aspect of this process is that porosity develops within individual particles, and it is not the consequence of particle spacing or gas entrapment *between* particles. A recent study [31] has shown that the particle size is an important aspect to the foaming rate, since porosity progresses inward from the surface, and larger particles require more time to fully foam (porosity to the center). Particle size is approximately 60 µm on average, and the pores created by the reduction and expansion of the dispersed oxide phase range from 10 µm to 50 nm or less.

The character and extent of the porosity was assessed using optical microscopy on polished sections of the foamed copper alloy. As shown in Figure 1, there are many small pores interspersed with larger voids. The large voids are created by particle boundaries remaining from incomplete compaction (~80% dense after uniaxial pressing to 2 GPa). Therefore, the largest porosity is not attributed to the foaming process, but is related to the compaction and sintering process. Because of the unique nature of this intraparticle expansion technique, there is an advantage to analyzing both the larger interparticle porosity as well as the porosity within the individual particles. This bimodal porosity is analyzed in the next few subsections, but the methods may be applied to any regular or stochastic porous material.

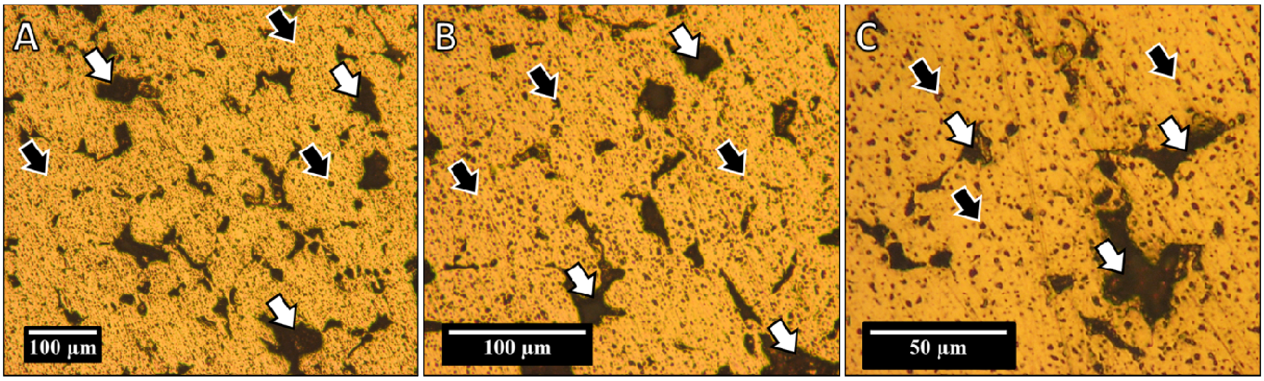

Figure 1. Optical microscopy performed on the polished cross-section of a powder compact at increasing magnification (A-C). Large voids (white arrows) represent incomplete compaction of the powder, not porosity created during the foaming process (black arrows).

3.1. Interparticle and intraparticle porosity using optical imaging

There are multiple microstructural length scales that can be observed in the metal foam shown in Figure 1 (i.e., larger interparticle voids as well as intraparticle porosity from the foaming process itself). Quantitative analysis of the largest length scale of the foamed microstructures can be easily performed from these optical microscopy images. In this analysis, approximately 20 images at multiple magnifications (see Figure 1) were analyzed to quantify the microstructure of these larger interparticle pores. Figure 2 details the multiple steps in the image segmentation procedure.

First, the image is converted to an 8-bit image (i.e., intensity 0–255), the background is leveled using quadratic functions in the x, y, and x-y directions, and the image intensity distribution is stretched to enhance contrast and normalize the intensities. Second, a binary mask is produced using a low threshold intensity value (e.g., 10) and a feature size criterion to produce the initial state for the active contour segmentation. The threshold value does not need to be precise, but rather it just needs to highlight pixels within the regions of the large interparticle pores (see Figure 2). Last, the active contour-based segmentation (a sparse-field level set method [33,34]) uses the binary mask image as a starting point and evolves the segmented regions to best capture the associated image (microstructure) features. The Chan-Vese method [35] was used for the active contour, i.e., the regions can either shrink or expand in an unbiased manner. As shown in Figure 2, this segmentation method performed well at capturing the large interparticle pores for subsequent quantitative analysis.

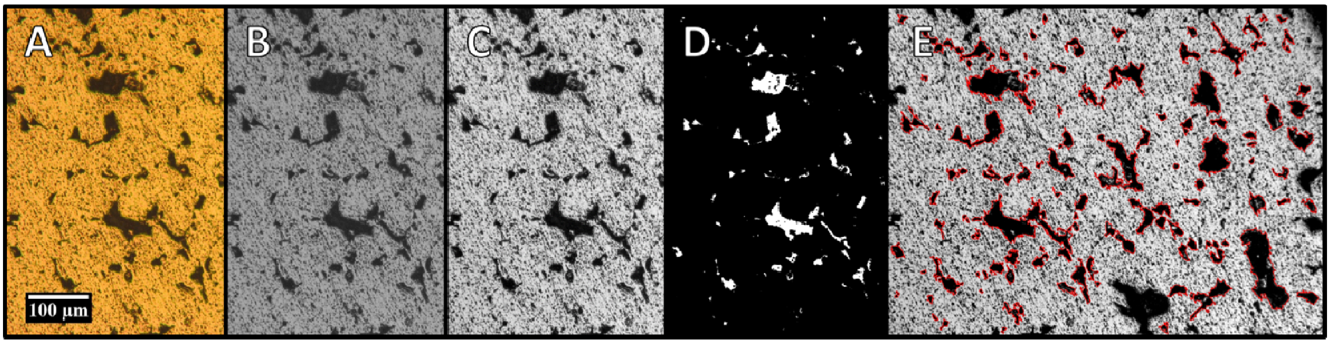

Figure 2. Image segmentation method utilized to segment the large microstructure features (e.g., porosity, voids) in the polished cross-section of a powder compact at increasing magnification. The different steps (from left to right) are: A) original optical image, B) conversion to 8 bit image, C) leveling the background and contrast stretch, D) initialize regions for active contour, and E) segmented features overlaid on original image after active contour segmentation.

The statistics can then be quantified and analyzed using the segmented microstructures. Figure 3 presents cumulative distribution function (CDF) plots of seven different normalized (between 0 and 1) properties of the segmented pores in the foamed Cu microstructures. These properties are 1) area, 2) eccentricity, 3) major and 4) minor axis lengths, 5) perimeter length, 6) solidity, and 7) equivalent diameter. The area, perimeter, major and minor axis lengths, and equivalent diameter are commonly used to quantify the morphology of different features. The eccentricity is the ratio of the distance between the foci of the ellipse and its major axis length with a value between 0 and 1 (i.e., 0 is a circle and 1 is a line segment). The solidity is the ratio of area of the region to that of the convex hull of the region (see Figure 4). The aforementioned segmentation procedure captured all of the large pores, but other techniques may be required to capture the smaller pores (to be discussed later).

The cumulative distribution plots show the corresponding percentiles and distribution shape for various properties of the different pores. The minimum and maximum values of the properties—corresponding to normalized values of 0 and 1, respectively—are listed in Table 1. The steep slope of many of the CDF plots (see Figure 3) indicates that the majority of the pores are small (low area, perimeter, major/minor axis length, and equivalent diameter) with a much smaller fraction of large pores. The lower initial slope of the eccentricity and solidity is because the pores tend to be elongated ellipses (eccentricity > 0.5 with a high solidity); both of these measures are independent of size.

Table 1. Minimum, mean, and maximum values of properties of segmented pores in the foamed microstructures.

Property	Minimum	Mean	Maximum
Area (μm^2)	0.08	32.0	8261.90
Eccentricity	0.00	0.71	0.98
Major Axis Length (µm)	0.37	5.50	363.50
Minor Axis Length (µm)	0.25	3.12	90.56
Perimeter (µm)	0.75	16.25	1255.50
Solidity (%)	0.33	0.92	1.00
Equivalent Diameter (µm)	0.31	3.79	102.56

It should be noted that Table 1 indicates a large difference between the minimum and maximum properties of the pores. For instance, the pore area changes by 5 orders of magnitude and the equivalent diameter by about 3 orders of magnitude. Much of this is due to the low magnification image (Figure 1A) containing more large pores while the higher magnification image (Figure 1C) contains much more of the smaller pores. The significance of these distributions is that this wide range of sizes and shapes is indicative of multiple length scales of porosity in this foamed material, specifically large interparticle pores and smaller intraparticle porosity.

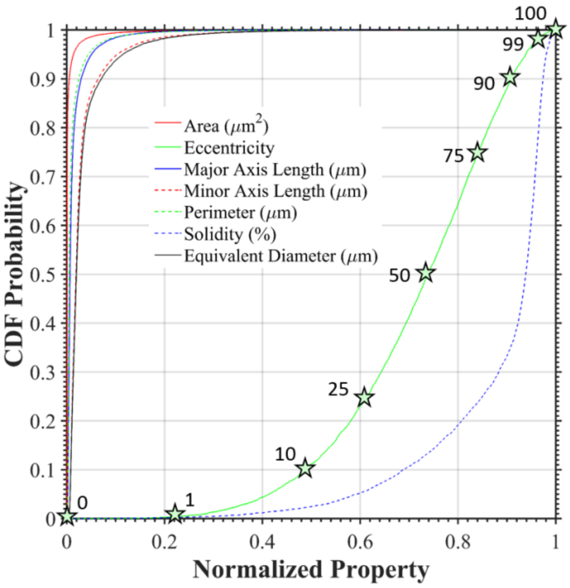

Figure 3. Cumulative distribution plot of normalized properties of segmented pores in the foamed microstructures, including area, eccentricity, major and minor axis lengths, perimeter length, and solidity. The stars and labels are examples of the nth percentile particles of the distribution, in association with particles from the low magnification images shown in Figure 4.

The range of the pore morphology within some of the low magnification optical images (Figure 1A) is shown in Figure 4. The pore size spans two orders of magnitude, and the majority of pores are small (i.e., the 50th percentile pore is closer in size to the minimum pore size than the maximum pore size). As an example of eccentricity, Figure 4B shows the nth percentile pore for eccentricity along with the extremes of this metric (0 is a circle, 1 is a line). As observed in Figure 3, very few pores are circular, and the majority of pores are elongated. Last, recall that the solidity is the ratio of the area of the pore to the area of the convex hull of the pore (i.e., an example of the convex hull is outlined in red for the 1st percentile pore in Figure 4C). As shown in Figure 4C, the large pores tend to have a low solidity, while the smaller pores are more "solid" (more convex-shaped). Note that solidity is defined by assuming the analyzed feature is a particle, not a void, and so a high solidity is actually associated with a greater ratio of open area in the real material. Pore analysis reveals that many of the pore properties are associated with being either interparticle (large, complicated morphology, low solidity) or intraparticle (small, ellipsoidal, high solidity). One strategy for fully characterizing these samples is to understand pores at multiple length scales, spanning from 100s of microns to the smallest resolvable sizes.

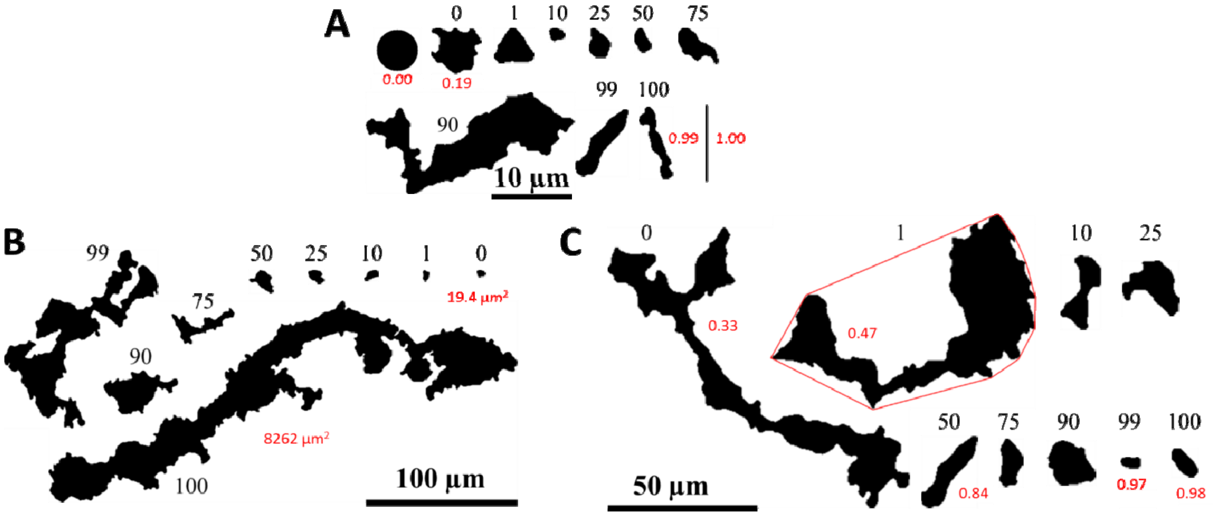

Figure 4. Pores associated with the nth percentile (in black) of the A) area, B) eccentricity, and C) solidity distributions for the low magnification optical images (see Figure 1A). Values of the properties are shown in red. The 0th and 100th percentile pores of the distribution correspond to the minimum and maximum properties. For solidity, the convex hull is shown in red for the 1st percentile pore.

3.2. Intraparticle porosity and microstructure using FIB tomography

To fully decouple porosity between and within particles and to improve resolution, SEM imaging can be used on individual particles. FIB tomography (or serial sectioning) can be used to generate two-dimensional surfaces within a single particle. This allows a cross-section to be created without structural damage, which may occur in abrasive polishing processes [36], though beam damage and artifacts are still concerns [37]. Some approaches used to reduce beam damage include the use of a sacrificial platinum deposition layer and a progressive reduction in milling intensity as the section reaches a finished condition. It was found that the porous nature of the samples reduced the benefits of a platinum layer, and the reduction of the ion beam current during final polishing was used solely. Even with this procedure, creating a smooth surface can be difficult due to the inhomogeneous microstructure of the material (i.e., pores, in this case) [38], and surface streaking (or "curtaining") is present as a consequence. SEM examination (Figure 5) of the particle cross-section confirms that microscale porosity exists in a range of sizes, and the pore morphology is irregular. At higher magnifications (e.g., Figure 5E), nanoscale porosity is also observed.

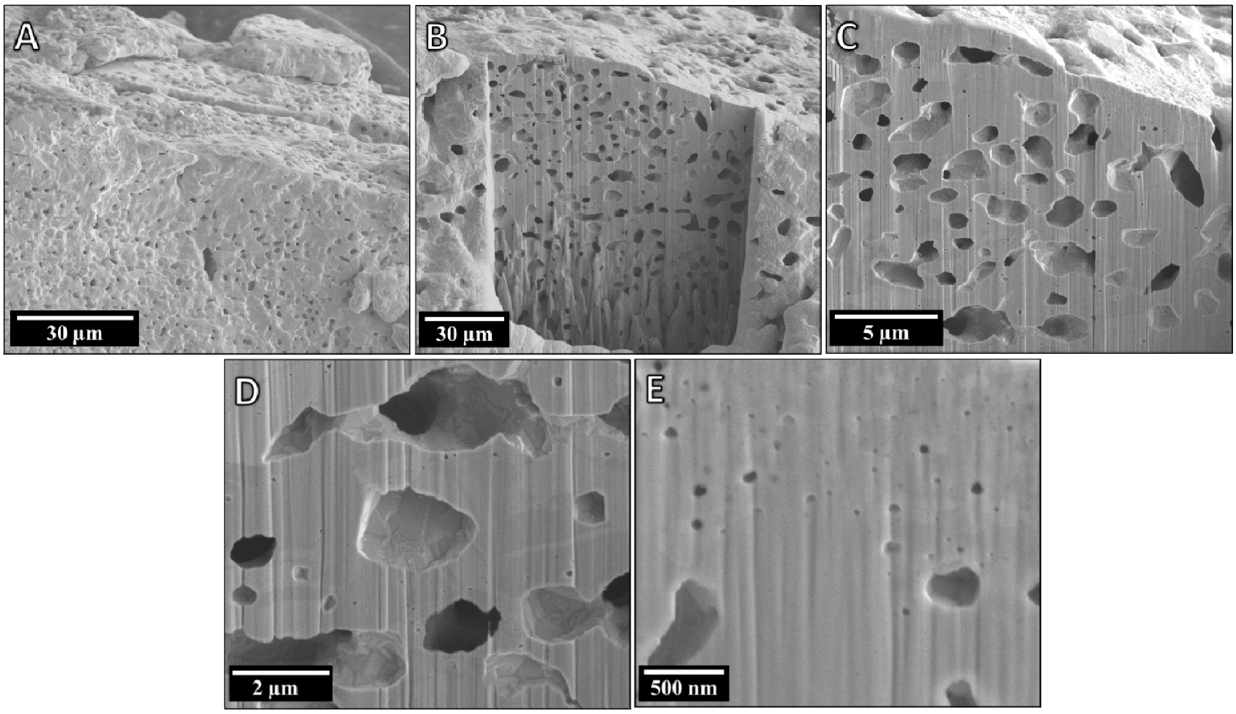

Figure 5. FIB cross-section of foamed Cu-Sb particle. Porosity is evident on the exterior of the particle (A), and FIB sectioning (B-E) reveals a distribution of pore sizes as well as the pore morphology.

Two-dimensional and three-dimensional pore statistics can be extracted from single particles as well. The methodology used for this follows a similar path to that described earlier: image preparation, segmentation of features, reduction to a binary image, and quantification of pores (e.g., Figure 2). By collecting and stacking a series of 2D images, a 3D structure can be generated. Visualization and quantification of this pore structure has shown [32] that the porosity within the particle is ~37%, the equivalent pore diameter is on the order of 1 µm with wall thicknesses on the same order of magnitude, the mean eccentricity is approximately 0.70 (similar to that in Table 1), and that greater than 90% of the pores are interconnected beneath the observed 2D image.

Here, the length scales associated with the pore structure and wall thickness of the foams is quantified using two-point statistics and lineal path functions. The two-point correlation function (TPCF) is the probability of two points distance r apart, lying within specified phases. This is sometimes normalized by their respective area/volume fractions f_1, where the subscript 1 refers to the phase (pore = 1, matrix = 2). The lineal path function (LPF) is the probability that a vector of length r lies completely within a single phase. It is noted that in both cases, the vector/distance r has a directionality component (θ) associated with it. In the following discussion, TPCFs and LPFs are denoted $P_{11}(r)$ and $L_{11}(r)$, respectively.

The difference between the TPCF, $P_{11}(r)$, and the LPF, $L_{11}(r)$, is schematically depicted in Figure 6. For this schematic, we chose a 1-D representation of 2 phases: the porosity phase in gray boxes and the matrix phase in white boxes. Figure 6 shows the combination of boxes that are accounted for in both $P_{11}(r)$ and LPF $L_{11}(r)$ for distances of $r = 1$, $r = 2$, and $r = 3$. First, notice that as the distance increases, the number of possible combinations for the TPCF increases. Again, the TPCF does not consider the boxes between end points, only the boxes at the ends of the line. In contrast, the LPF requires that *all* boxes along the line belong to a particular phase, and therefore, the probability of a line encountering only a single phase decreases with increasing length. Additionally, this schematic shows that the TPCF represents the spacing between porosity while the LPF represents the connectivity of porosity. This concept was applied to a previously reconstructed 3D reconstructed foamed microstructure [32] from an individual particle to assess the length scales of the porosity and matrix "phases".

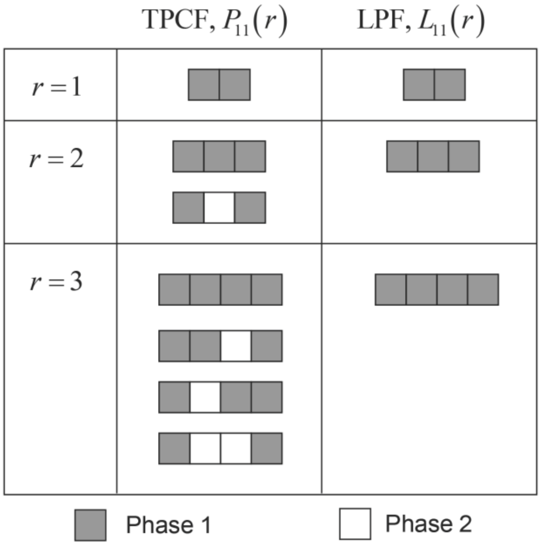

Figure 6. One dimensional schematic showing the difference between two-point correlation functions and lineal path functions for distances of 1, 2, and 3 pixels.

The length scales of the microstructure can then be assessed from these statistics, and Figure 7 shows an example of how the TPCF evolves as a function of distance for (A) multiple slices and (B) multiple orientations. Notice that the TPCF is divided by the square of the area/volume fraction of porosity such that the normalized TPCF approaches 1 at large distances. This makes sense; at large distances where you would not expect any correlation, the probability of pixels at distance *r* both lying within one phase is simply related to the probability that either pixel is that phase (i.e., the area/volume fraction f_1). At short distances, however, the TPCF can provide useful information about the length scale associated with the microstructure. For instance, as shown in Figure 7B, a criterion of 10% or 50% above the converged TPCF at large distances (i.e., $P_{11} = 1.1$ or $P_{11} = 1.5$, respectively) can be used to define a length scale of a particular microstructural feature over multiple directions (to indicate the degree of anisotropy of microstructure).

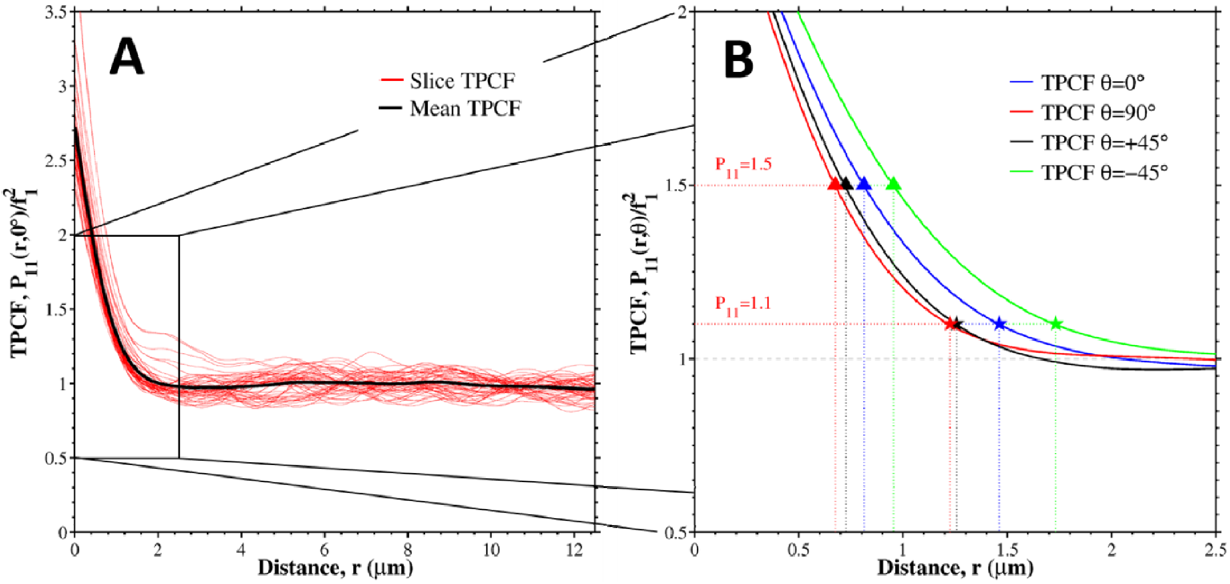

Figure 7. Normalized two-point correlation function $P_{11}(r)$ plot for porosity as a function of distance (a) for individual slices through a foamed particle and the mean behavior, and (b) along different directions (given by θ) within the microstructure.

In a similar manner, the lineal path function (Figure 8) converges to 0 as the distance increases; that is, there is eventually no (or little) probability of a line of length *r* completely lying within a particle phase given a particular length scale of the microstructure. In this respect, the length scale can be assessed from the LPF by using a criterion based on the (n^{th} percentile) probability that a line of length *r* will completely lie within a phase, i.e., 10%, 25%, 50% lie in that phase. Figure 8 shows the lineal path function as a function of line length for all slices in the 3D dataset as well as the mean behavior for one direction in the microstructure (in this case, 0°). The corresponding line length (i.e., length scale) for 1%, 10%, 25%, and 50% occurrence are shown by dotted lines in the plots and their length scale values are listed.

The length scales based on these various criteria for TPCF and LPF is given in Table 2. As shown in Figure 7B, the length scale depends on both the orientation and the phase being considered. In general, both the TPCF and LPF criteria give length scales that are on the order of 1–2 μm. The LPF statistics suggest that the matrix length scale is larger than the pore length scale, on the order of 3–4 times. Additionally, by comparing the 0° with the 90° LPF length scales, this trend is fairly isotropic within the microstructure. Recall that L_i = 25% is the length scale where 25% of lines randomly placed in the microstructure will fall within the particular phase. This is also reflected in the TPCF length scales; the matrix length scales are noticeably smaller than the pore length scales (i.e., the matrix converges more rapidly to a critical spacing than the porosity). Both of these length scales are influenced by the area/volume fraction of the porosity or matrix.

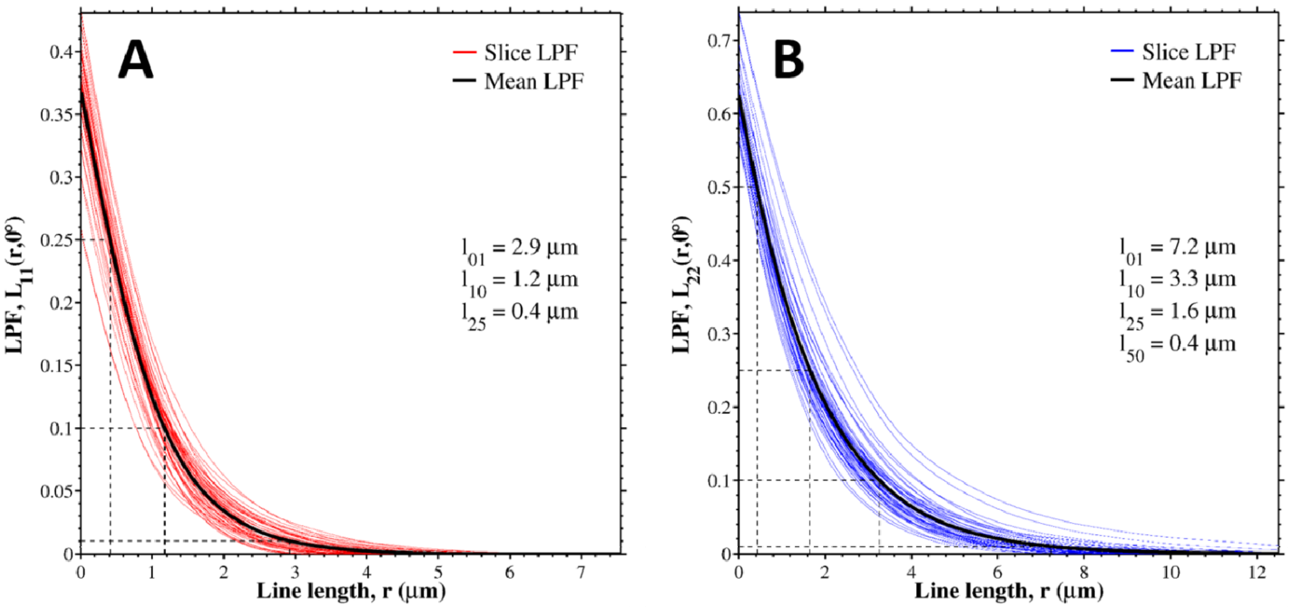

Figure 8. Lineal Path Function (LPF) as a function of line length (r) for (a) the porosity, i.e., L_{11}(r, 0°) and (b) the matrix, i.e., L_{22}(r, 0°). The colored lines are the LPF computed from individual slices (red for porosity, blue for matrix) and the dashed lines show the line length (scales) for particular probabilities of occurrence within the LPF (1%, 10%, 25%, 50%).

Table 2. Length scales of pores and Cu matrix in the foamed particle microstructures for different TPCF and LPF criteria.

Two-Point Correlation Function Analysis								
Phase	Length Scale *r* (μm) @ P_{ii}=1.1				Length Scale *r* (μm) @ P_{ii}=1.5			
	0°	45°	90°	-45°	0°	45°	90°	-45°
Pore (i=1)	1.46	1.23	1.26	1.73	0.81	0.68	0.72	0.95
Matrix (i=2)	1.08	0.88	0.94	1.24	0.16	0.14	0.16	0.19

Lineal Path Function Analysis						
Phase	Length Scale *r* (μm) @ L_i=0.1		Length Scale *r* (μm) @ L_i=0.25		Length Scale *r* (μm) @ L_i=0.50	
	0°	90°	0°	90°	0°	90°
Pore (i=1)	1.2	1.4	0.4	0.5	N/A	N/A
Matrix (i=2)	3.3	3.9	1.6	2.0	0.4	0.5

These methods of sectioning, image segmentation and statistical analysis can be applied to images generated through various methods (e.g., mechanical polishing, FIB milling, etc.), at varying length scales and to 2D and 3D structures. The method chosen to characterize the material is important for more than just the pore morphology. A benefit of FIB sectioning is the ability to perform site-specific characterization on 2D surfaces and to generate 3D reconstructions. In addition to milling, the FIB beam can also be used to generate ion-channeling contrast (ICC) images. The differing grain orientations result in a commensurate deviation in the signal intensity received by the detector, and therefore can be used to assist in identifying grain size. A FIB ICC image of the sectioned foam is shown in Figure 9A. This combination offers direct correlation between the pore morphology and microstructure within the material.

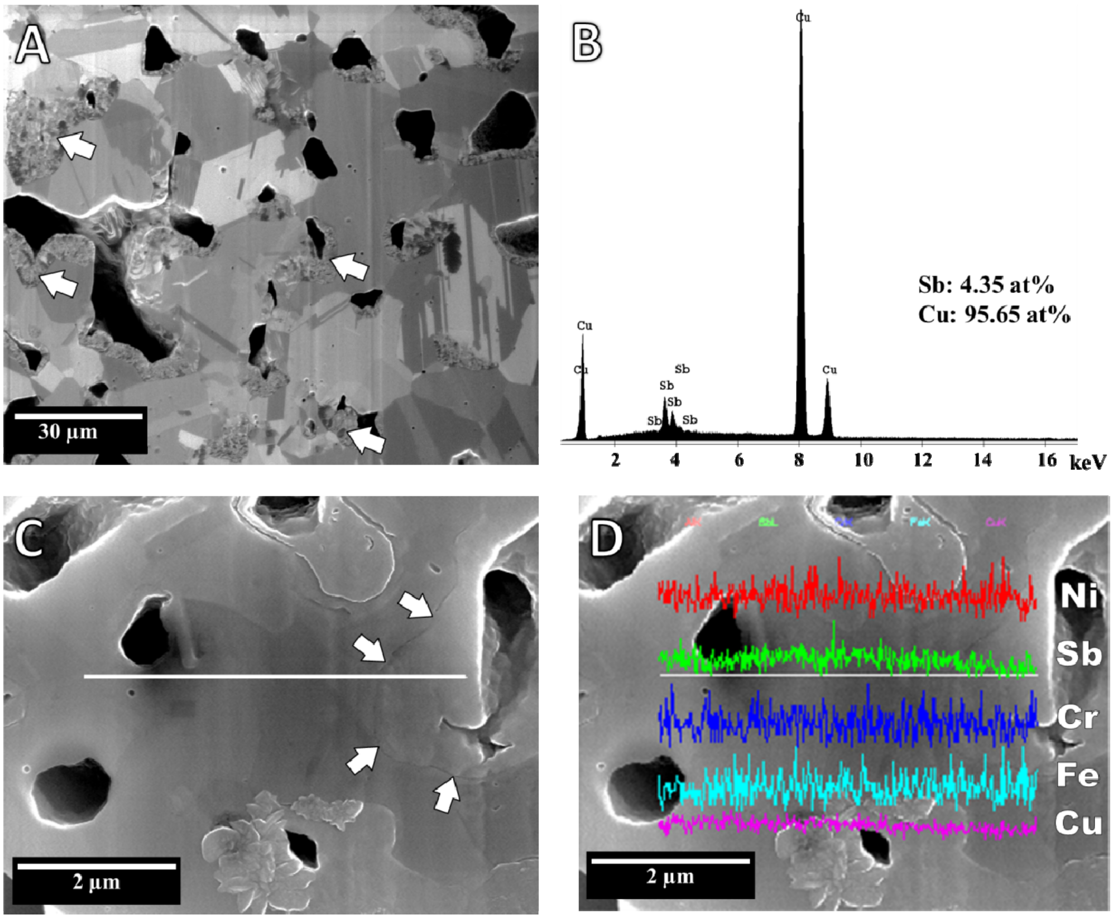

Figure 9. FIB sectioning allows for site-specific analysis using multiple methods. (A) Ion-channeling contrast (ICC) reveals a fine grain size combined with regions of nanoscale grains (identified by white arrows). (B) Chemical verification by EDS analysis of a large area of the sample confirms the presence of Cu and Sb in the expected atomic ratios. (C) Secondary electron image of fine grained and nanostructured regions (boundary noted by white arrows) identified in (A) are subjected to an EDS line scan, and (D) the line scan reveals no compositional difference between fine-grained and nanostructured regions.

ICC imaging reveals that the matrix has a fine grain size overall, with some areas exhibiting nanostructured characteristics (see white arrows in Figure 9A). High-energy ball milling, as used here, is capable of creating nanocrystalline metals and alloys [39–45], but retaining nanoscale grains at the annealing/foaming temperature of 600 °C would require a stabilized structure (e.g., [46–49]). Sb has been studied as a grain size stabilizer for copper [50–53], but was found ineffective when added up to 1 at%. The larger concentration used here (5 at%) may result in segregation of the Sb to grain boundaries and surfaces due to its insolubility at room temperature [54,55] and provide the necessary presence to retain nanoscale grains.

Because FIB sectioning can be combined with other, *in situ* analysis, chemical verification by EDS analysis can be performed at areas of interest as soon as they are identified. An area scan of the sample (Figure 9B) confirms the presence of Cu and Sb in the expected atomic ratios without appreciable contamination. To determine whether the nanostructured regions are enriched in Sb, a line scan extending from the fine-grained interior to the nanostructured region was used (see Figure 9C). The fine-grained and nanostructured regions are only faintly visible in the secondary electron images (Figure 9C, D), and the elemental line scan reveals no significant change in composition from one area to the next, including possible contaminants from the milling process (i.e., Fe, Cr and Ni). Note that the vertical placement of the elements identified in Figure 9d are arbitrary, and only Cu and Sb were identified in appreciable quantities. The lack of compositional difference between fine-grained and nanostructured regions, and the fact that these regions are exclusively located along pore surfaces, suggests that this is a redeposition of material during the FIB milling process [37]. This highlights the balance between benefits and concerns in this type of analysis, as well as the importance of thorough examination.

4. Discussion

Foamed metals retain some of the most attractive qualities of metals while also effectively reducing their characteristically high density. Metallic properties can then be paired with much lower density, high specific surface area, tailored thermal and acoustic properties, efficient energy absorption, constant crushing load, etc. [1–5,56]. Manufacturing techniques that ensure these materials possess the required characteristics can only be developed and monitored through efficient and accurate characterization. As pore size decreases into the micron and nanoscale regime, advanced methods of characterization are needed.

The most basic two-dimensional characterization method for metallic foams is cross-sectional examination by optical microscopy (e.g., [25,26,57]). Unfortunately, in stochastic foams which possess nanoscale pores, this method is insufficient to create a holistic understanding of the size and morphology, even though the majority of microscale pore volume can be resolved. In cases where the porosity is entirely nanoscale (e.g., [11,58,59]), optical methods are unsuitable. To characterize sub-micron and nanoscale porosity alternative techniques such as electron microscopy by SEM [29,59,60] and TEM [11,13] are beneficial.

All of these methods are valuable tools in determining the characteristics of porosity, but they provide two-dimensional information about a three-dimensional structure. For that reason, the most comprehensive characterization will involve methods which can examine the entire pore volume. These methods vary greatly in their applications and ease of use. Traditional, abrasive polishing can be used to reconstruct 3D microstructures using automated equipment (e.g., [61]). The advantages include the ability to observe large areas quickly while maintaining good resolution (slices of hundreds of nanometers or microns). This process is suitable for metallic foams with pore sizes large enough to be fully resolved by optical microscopy (millimeter to micron range).

To address the challenge of sub-micron and nanoscale porosity, methods such as high-resolution X-ray tomography [62–65], transmission electron tomography [66,67] and FIB serial sectioning [31,32,68–71] can be used. The benefit of X-ray and electron tomographic characterization is that it can provide detailed volumetric information in a nondestructive manner, and can even be used to assess materials during *in situ* deformation [63].

FIB tomography (or serial sectioning) also provides valuable, volumetric information to examine a variety of microstructural features [37,72]. For instance, it can be used to assess phase distributions [73,74,75], grain structure [71,76], and even biological and geological specimens [77,78]. The sample volume is typically limited to micrometer dimensions, but can achieve resolution in 10s of nanometers, giving it higher resolution than X-ray tomography, but lower than TEM tomography.

Despite the diverse applications FIB tomography is applied towards, there is relatively little work on porous materials. With dual beam microscopes becoming increasingly common, this method is thought to present a valuable option for analyzing and reconstructing micro- and nanoporous materials by serial sectioning. When combined with analysis such as electron back scatter diffraction (EBSD), ICC and/or EDS (including area mapping), the material can be simultaneously assessed with regard to pore size, volume and morphology, grain size and orientation, and elemental content and distribution. Porous structures created by the AERO process may have important features regarding all of these aspects, and a complete description requires a multi-faceted approach to characterization.

The analysis utilized here provides a relatively simple method for generating a quantitative description of porosity. Although these methods are applicable to any porous material, this approach is especially important in materials which do not have regular pore geometries and exhibit a range of pore sizes. The AERO foaming process provides a unique combination of characterization challenges because of its structure, and a detailed investigation requires multiple techniques. In previous work [32], FIB serial section was used to analyze and reconstruct porosity in three-dimensions. Here two-dimensional sections of much greater area were analyzed to provide a complementary data set which displayed similar results of pore morphology to the 3D analysis, though with less overall information. Depending on the pore characteristics and the level of detail required, characterization and image analysis techniques can be chosen which efficiently provide data. By combining methods suited for multiple length scales and which incorporate additional utility, such as crystallographic and elemental analysis, a comprehensive understanding of the microstructure can be achieved.

5. Conclusion

The challenges and opportunities associated with characterizing micro- and nanoscale stochastic porosity have been identified and demonstrated using a unique metallic foam created through solid state processing. The attributes of the foam were assessed using mechanical polishing and optical microscopy as well as focused ion beam cross-sectioning. The majority of pore volume is made up of microscale pores which can be resolved in the optical images, but the porosity cannot be fully described since many pores are sub-micron and nanoscale. FIB sectioning reveals these pores in two-dimensional surfaces and allows three-dimensional analysis to be accomplished tomographically. Pore characteristics were assessed in regard to factors such as solidity, eccentricity, equivalent area and perimeter using image processing and statistical analysis. In compacted and sintered samples it was found that pores within powder particles tend to be convex (high solidity) and those between particles are irregular with a low solidity. The capabilities of various characterization methods for porous materials were also described, and in particular, methods which also incorporate elemental or microstructural analysis are seen as being quite valuable to developing a holistic understanding of the material.

Conflict of Interest

All authors declare no conflicts of interest in this paper.

References

1. Banhart J (2001) Manufacture, characterisation and application of cellular metals and metal foams. *Prog Mater Sci* 46: 559–632.
2. Banhart J (2013) Light-Metal Foams - History of Innovation and Technological Challenges. *Adv Eng Mater*15: 82–111.
3. Ashby MF, Evans AG, Fleck NA, et al. (2000) Metal Foams: A Design Guide. Boston: Butterworth-Heineman.
4. Lefebvre L-P, Banhart J, Dunand DC (2008) Porous Metals and Metallic Foams: Current Status and Recent Developments. *Adv Eng Mater* 10: 775–787.
5. Ashby MF, Tianjian LU (2003) Metal foams: A survey. *Science In China* (Series B) 46: 521–532.
6. Banhart J (2007) Metal Foams - from Fundamental Research to Applications. In: Raj B, Ranganathan S, Rao KBS, Matthew MD, Shankar P, eds. Frontiers in the Design of Materials: Universities Press (India).
7. Banhart J (2006) Metal Foams: Production and Stability. *Adv Eng Mater* 8:781–794.
8. Ashby MF (1983) Mechnical properties of cellular solids. *Metallurgical Transactions A* 14A: 1755–1769.
9. Davies GJ, Zhen S (1983) Metallic foams: their production, properties and applications. *J Mater Sci* 18: 1899–1911.
10. Garcia-Avila M, Rabiei A (2015) Effect of Sphere Properties on Microstructure and Mechanical Performance of Cast Composite Metal Foams. *Metals* 5: 822–835.
11. Shin H-C, Dong J, Liu M (2003) Nanoporous Structures Prepared by an Electrochemical Deposition Process. *Adv Mater* 15:1610–1614.
12. Shin H-C, Liu M (2004) Copper Foam Structures with Highly Porous Nanostructured Walls. *Chem Mater* 16: 5460–5464.
13. Nam D, Kim R, Han D, et al. (2011) Effects of (NH4)2SO4 and BTA on the nanostructure of copper foam prepared by electrodeposition. *Electrochim Acta* 56: 9397–9405.
14. Kim JH, Kim RH, Kwon HS (2008) Preparation of copper foam with 3-dimensionally interconnected spherical pore network by electrodeposition. *Electrochemistry Communications* 10: 1148–1151.
15. Kennedy A (2012) Porous Metals and Metal Foams Made from Powders. In: Kondoh K, ed. Powder Metallurgy Rijeka,Croatia InTech.
16. Torres Y, Pavón JJ, Rodríguez JA (2012) Processing and characterization of porous titanium for implants by using NaCl as space holder. *J Mater Process Tech* 212: 1061–1069.
17. Wenjuan N, Chenguang B, GuiBao Q, et al. (2009) Processing and properties of porous titanium using space holder technique. *Mater Sci Eng A* 506: 148–151.
18. Xie S, Evans JRG (2004) High porosity copper foam. *J Mater Sci* 39: 5877–5880.

19. Torres Y, Lascano S, Bris J, et al. (2014) Development of porous titanium for biomedical applications: A comparison between loose sintering and space-holder techniques. *Mat Sci Eng C* 37: 148–155.
20. Laptev A, Bram M, Buchkremer HP, et al. (2004) Study of production route for titanium parts combining very high porosity and complex shape. *Powder Metallurgy* 47: 85–92.
21. Paserin V, Marcuson S, Shu J, et al. (2004) CVD technique for Inco nickel foam production. *Adv Eng Mater* 6: 454–459.
22. Hodge AM, Biener J, Hsiung LL, et al. (2005) Monolithic nanocrystalline Au fabricated by the compaction of nanoscale foam. *J Mater Res* 20: 554–557.
23. Tai MC, Gentle A, Silva KSBd, et al. (2015) Thermal Stability of Nanoporous Raney Gold Catalyst. *Metals* 5: 1197–1211.
24. Lin B, Kong L, Hodgson PD, et al. (2014) Impact of the De-Alloying Kinetics and Alloy Microstructure on the Final Morphology of De-Alloyed Meso-Porous Metal Films. *Nanomaterials* 4: 856–878.
25. Davis NG, Teisen J, Schuh C, et al. (2001) Solid-state foaming of titanium by superplastic expansion of argon-filled pores. *J Mater Res* 16: 1508–1519.
26. Dunand DC. (2004) Processing of Titanium Foams. *Adv Eng Mater* 6: 369–376.
27. Elzey DM, Wadley HNG (2001) The Limits Of Solid State Foaming. *Acta Mater* 49: 849–859.
28. Kearns MW (1987) inventor Formation of Porous Bodies patent 4,659,546.
29. Oppenheimer S, Dunand DC (2010) Solid-state foaming of Ti–6Al–4V by creep or superplastic expansion of argon-filled pores. *Acta Mater* 58: 4387–4397.
30. Li H, Oppenheimer SM, Stupp SI, et al. (2004) Effects of Pore Morphology and Bone Ingrowth on Mechanical Properties of Microporous Titanium as an Orthopaedic Implant Material. *Mater T JIM* 45: 1124–1131.
31. Atwater MA, Darling KA, Tschopp MA (2016) Solid-State Foaming by Oxide Reduction and Expansion: Tailoring the Foamed Metal Microstructure in the Cu–CuO System with Oxide Content and Annealing Conditions. *Adv Eng Mater* 18: 83–95.
32. Atwater MA, Darling KA, Tschopp MA (2014) Towards Reaching the Theoretical Limit of Porosity in Solid State Metal Foams: Intraparticle Expansion as a Primary and Additive Means to Create Porosity. *Adv Eng Mater* 16: 190–195.
33. Caselles V, Kimmel R, Sapiro G (1997) Geodesic active contours. *Int J Comput Vision* 22: 61–79.
34. Whitaker RT (1998) A level-set approach to 3d reconstruction from range data. *Int J Comput Vision* 29: 203–231.
35. Chan TF, Vese LA (2001) Active contours without edges. *IEEE T Image Process* 10: 266–277.
36. Samuels LE (2003) Metallographic Polishing by Mechanical Methods. 4th ed. Materials Park, OH: ASM International.
37. Mingard KP, Jones HG, Gee MG (2013) Metrological challenges for reconstruction of 3-D microstructures by focused ion beam tomography methods. *J Microsc* 253: 93–108.
38. Volkert CA, Minor AM (2007) Focused Ion Beam Microscopy and Micromachining. *MRS Bull* 32: 389–395.
39. Suryanarayana C, Ivanob E, Boldyrev VV. (2001) The science and technology of mechanical alloying. *Mater Sci Eng A* 304–306:151–158.
40. Suryanarayana C (2001) Mechanical alloying and milling. *Prog Mater Sci* 46:1–184.
41. Suryanarayana C, Koch CC (2000) Nanocrystalline materials – Current research and future directions. *Hyperfine Interact* 130:5–44.

42. Koch CC (1989) Materials synthesis by mechanical alloying. *Annu Rev Mater Sci* 19: 121–143
43. Koch CC (1993) The synthesis and structure of nanocrystalline materials produced by mechanical attrition: A review. *Nanostruct Mater* 2: 109–129.
44. Koch CC, Cho YS (1992) Nanocrystals by high energy ball milling. *Nanostruct Mater* 1: 207–212.
45. Lü L, Lai MO (1998) Mechanical alloying. Boston: Kluwer Academic Publishers.
46. Krill CE, Klein R, Janes S, et al. (1995) Thermodynamic stabilization of grain boundaries in nanocrystalline alloys. *Mater Sci Forum* 181: 443–448.
47. Koch CC, Scattergood RO, Darling KA, et al. (2008) Stabilization of nanocrystalline grain sizes by solute additions. *J Mater Sci* 43: 7264–7272.
48. Trelewicz JR, Schuh CA (2009) Grain boundary segregation and thermodynamically stable binary nanocrystalline alloys. *Phys Rev B* 79:1–13.
49. Li J, Wang J, Yang G (2009) On the stagnation of grain growth in nanocrystalline materials. *Scripta Mater* 60: 945–948.
50. Rajgarhia RK, Saxena A, Spearot DE, et al. (2010) Microstructural stability of copper with anitmony dopants at grain boundaries: experiments and molecular dynamics simulations. *J Mater Sci* 45: 6707–6718.
51. Rajgarhia RK, Spearot DE, Saxena A (2010) Plastic deformation of nanocrystalline copper-antimony alloys. *J Mater Res* 25: 411–421.
52. Rajgarhia RK, Spearot DE, Saxena A. (2010) Behavior of dopant-modified interfaces in metallic nanocrystalline materials. *JOM* 62: 70–74.
53. Atwater MA, Mula S, Scattergood RO, et al. (2013) Thermal Stability of Nanocrystalline Copper Alloyed with Antimony. *Metall Mater Trans A* 44: 5611–5616.
54. Liu XJ, Wang CP, Ohnuma I, et al. (2000) Thermodynamic assessment of the phase diagrams of the Cu-Sb and Sb-Zn systems. *J Phase Equilib* 21: 432–442.
55. MSIT®, Bätzner C, Ferro R, et al. (2007) Cu-Sb-Zn (Copper-Antimony-Zinc). In: Ilyenko GES, ed. Non-Ferrous Metal Ternary Systems Selected Copper Systems: Phase Diagrams, Crystallographic and Thermodynamic Data: Springer-Verlag.
56. Banhart J, Baumeister J (1998) Production Methods for Metallic Foams. *MRS Proceedings* 521.
57. Murray NGD, Dunand DC. (2003) Microstructure evolution during solid-state foaming of titanium. *Compos Sci Technol* 63: 2311–2316.
58. Zhang Z, Wang Y, Qi Z, et al. (2009) Generalized Fabrication of Nanoporous Metals (Au, Pd, Pt, Ag, and Cu) through Chemical Dealloying. *J Phys Chem C* 113: 12629–12636.
59. Cheng I-C, Hodge A (2013) Strength scale behavior of nanoporous Ag, Pd and Cu foams. *Scripta Mater* 69: 295–298.
60. Liu R, Antoniou A (2012) A relation between relative density, alloy composition and sample shrinkage for nanoporous metal foams. *Scripta Mater* 67: 923–926.
61. Spowart JE (2006) Automated serial sectioning for 3-D analysis of microstructures. *Scripta Mater* 55: 5–10.
62. Bart-Smith H, Bastawros A-F, Mumm DR, et al. (1998) Compressive deformation and yielding mechanisms in cellular Al alloys determined using X-ray tomography and surface strain mapping. *Acta Mater* 46: 3583–3592.
63. Maire E (2012) X-Ray Tomography Applied to the Characterization of Highly Porous Materials. *Ann Rev Mater Res* 42: 163–178.

64. Rack A, Haibel A, Bütow A, et al. Characterization of Metal Foams with Synchrotron Tomography and 3D Image Analysis. 16th World Conference on Nondestructive Testing.
65. Elmoutaouakkil A, Salvo L, Maire E, et al. (2002) 2D and 3D Characterization of Metal Foams Using X-ray Tomography. *Adv Eng Mater* 4: 803–807.
66. Midgley PA, Weyland M, Yates TJV, et al. (2006) Nanoscale scanning transmission electron tomography. *J Microsc* 223: 185–190.
67. Rösner H, Parida S, Kramer D, et al. (2007) Reconstructing aNanoporousMetal in Three Dimensions: An Electron Tomography Study of Dealloyed Gold Leaf. *Adv Eng Mater* 9: 535–541.
68. Tschopp MA, Darling KA, Atwater MA (2014) Surpassing the Theoretical Limit of Porosity in Conventional Solid-State Foaming: Microstructure Characterization of Length Scales in a Copper Metal Foam. Army Research Laboratory, ARL-TR-7139.
69. VanLeeuwen BK, Darling KA, Koch CC, et al. (2011) Novel technique for the synthesis of ultra-fine porosity metal foam via the inclusion of condensed argon through cryogenic mechanical alloying. *Mater Sci Eng A* 528: 2192–2195.
70. Vázquez M, Moore D, He X, et al. (2014) Focussed ion beam serial sectioning and imaging of monolithic materials for 3D reconstruction and morphological parameter evaluation. *Analyst* 139: 99–104.
71. Xu W, Ferry M, Mateescu N, et al. (2007) Techniques for generating 3-D EBSD microstructures by FIB tomography. *Mater Charact* 58: 961–967.
72. Kubis AJ, Shiflet GJ, Dunn DN, et al. (2004) Focused Ion-Beam Tomography. *Metall Mater Trans A* 35:1935–1943.
73. Yazzie KE, Williams JJ, Phillips NC, et al. (2012) Multiscale microstructural characterization of Sn-rich alloys by three dimensional (3D) X-ray synchrotron tomography and focused ion beam (FIB) tomography. *Mater Charact* 70: 33–41.
74. Vivet N, Chupin S, Estrade E, et al. (2011) 3D Microstructural characterization of a solid oxide fuel cell anode reconstructedby focused ion beam tomography. *J Power Sources* 196: 7541–7549.
75. Nagasekhar AV, Cáceres CH, Kong C (2010) 3D characterization of intermetallics in a high pressure die cast Mg alloy using focused ion beam tomography. *Mater Charact* 61: 1035–1042.
76. West GD, Thomson RC (2009) Combined EBSD/EDS tomography in a dual-beam FIB/FEG–SEM. *J Microsc* 233: 442–450.
77. Winter DAMd, Schneidenberg CTWM, Lebbink MN, et al. (2009) Tomography of insulating biological and geological materials using focused ion beam (FIB) sectioning and low-kV BSE imaging. *J Microsc* 233: 372–383
78. Kizilyaprak C, Daraspe J, Humbel BM (2014) Focused ion beam scanning electron microscopy in biology. *J Microsc* 254: 109–114.